Infiltration into fractured bedrock

Rohit Salve and Teamrat A. Ghezzehei

Earth Sciences Division, Lawrence Berkeley National Laboratory, Berkeley, California, USA.

Robert Jones

Earth Sciences Division, Sandia National Laboratories

Rohit Salve and Teamrat A. Ghezzehei, Earth Sciences Division, Lawrence Berkeley National Laboratory, Berkeley, California, USA (R_Salve@lbl.gov, TAGhezzehei@lbl.gov), Robert Jones, Earth Sciences Division, Sandia National Laboratories

Abstract. One potential consequence of global climate change and rapid changes in land use is an increased risk of flooding. Proper understanding of floodwater infiltration thus becomes a crucial component of our preparedness to meet the environmental challenges of projected climate change. In this paper, we present the results of a long-term infiltration experiment performed on fractured ash flow tuff. Water was released from a 3×4 m^2 infiltration plot (divided into 12 square subplots) with a head of $\sim$0.04 m, over a period of $\sim$800 days. This experiment revealed peculiar infiltration patterns not amenable to current infiltration models, which were originally developed for infiltration into soils over a short duration. In particular, we observed that in part of the infiltration plot, the infiltration rate abruptly increased a few weeks into the infiltration tests. We suggest that these anomalies result from increases in fracture permeability during infiltration, which may be caused by swelling of clay fillings and/or erosion of infill debris. Interaction of the infiltration water with subsurface natural cavities (lithophysal cavities) could also contribute to such anomalies. This paper provides a conceptual model that partly describes the observed infiltration patterns in fractured rock and highlights some of the pitfalls associated with direct extension of soil infiltration models to fractured rock over a long period.

1. Introduction

According to a recent report by the Intergovernmental Panel on Climate Change (IPCC), "[. . . g]lobal warming is likely to lead to greater extremes of drying and heavy rainfall and increase the risk of droughts and floods [. . .]" [*Albritton et al.*, 2001]. Moreover, the ongoing rapid change in land use will likely aggravate the risk of increased flooding even further. The standing waters created by such extreme weather events, which typically cover vast areas, pose major environmental and health risks. Thus, drainage of these waters is usually one of the major post-disaster recovery challenges. When engineered drainage is not feasible, prediction of natural infiltration of the standing waters over extended periods of flooding (several weeks to months) becomes a crucial component of recovery management [*Pilon*, 2004].

The current concepts and theories of infiltration were originally developed to describe the process of water entry into soil-mantled landscapes over relatively short periods (at most, several days of rain) [*Hillel*, 1998]. A review of the basic principles that govern infiltration in soils is given by *Philip* [1969]. Experiments and modeling studies involving a shallow pond of water instantaneously applied on the surface of an initially dry soil indicate that infiltration starts out at a high rate and gradually decreases, asymptotically approaching a steady-state infiltration rate [e.g., *Elrick et al.*, 1995; *Philip*, 1992; *Youngs*, 1995]. The decrease in infiltration rate could be caused by deterioration of the soil structure (e.g., collapse of aggregates and swelling of clays). However, the major cause for the decrease in infiltration rate is the weakening of the matric potential gradient. Initially, the gradient is high because of the large difference in potential between the saturated surface

soil and the dry soil just ahead of the wetting front over a short distance. With time, as the wetting front deepens, the same potential difference acts across a thicker soil profile, resulting in a potential gradient that decreases with time. When the ponded surface is very large and the soil is homogeneous, the steady-state infiltration rate is equivalent to the saturated hydraulic conductivity.

In contrast to soils, studies on infiltration into exposed fractured bedrock are very limited in number and scope. Many studies of flow and transport in fractured vadose zones treat infiltration as a constant-rate boundary condition [e.g., *Glass et al.*, 2002]. Field experiments and modeling studies of infiltration over exposed fractured basalt performed at Idaho National Laboratory (INL, formerly Idaho National Environmental and Engineering Laboratory) [*Faybishenko et al.*, 1998; *Unger et al.*, 2004; *Wood and Norell*, 1996] indicate that the short-term average infiltration pattern is similar to what is expected in soils. In contrast, controlled infiltration tests along a single exposed fracture on chalk revealed that the infiltration behavior is highly erratic and far from the gradual decrease predicted by the soil infiltration models [*Dahan et al.*, 1999, 2000].

Recently, *Salve* [2005] reported results of long-term liquid-release tests performed at Yucca Mountain (a site that is being investigated by the U.S. Department of Energy as a potential nuclear waste repository). The goal of the study was to identify and characterize flow paths that developed as water was released under ponded conditions along a 12 m^2 infiltration plot as it traversed over 20 m of fractured rock mass.

In this paper, we revisit the results of *Salve* [2005] with emphasis on interpretations of the observed infiltration patterns, in the context of flooding of exposed fractured bedrock in regions that normally experience little precipitation. This effort differs from work pre-

sented by *Salve* [2005] in that it addresses near-surface processes associated with ponded infiltration, rather than on features of flow paths (such as flow velocities, size, spatial distribution and temporal dynamics). Specifically, we highlight some anomalous infiltration temporal patterns observed in some of the infiltration subplots and examine the significance of these anomalies to floodwater drainage. It must be clear from the outset that the analyses presented herein are not intended to, nor appropriate for, describing surface infiltration processes at Yucca Mountain, which is located in a dry climate with rugged topography, with very low likelihood of long periods of surface flooding.

2. Methods

A detailed account of the objectives and design of the field tests that generated the data we are concerned with in this paper is given by *Salve* [2005]. Highlights of the experimental portions that are relevant to this paper are given below.

Water was released over a horizontal surface of fractured welded tuff over a period of 25 months, during which the spatial and temporal variability in infiltration rates were continuously monitored. In addition to the ponded release of water, subsections of the infiltration zone were also perturbed by interruptions to the supply of water and alterations to the plot surface. Observations from this extended infiltration event, with sporadic disruptions, were then analyzed to elucidate mechanisms that influenced the rate at which water moved through the fractured rock surface.

2.1. Study Site

The test bed is located 190 m below the ground surface of Yucca Mountain, where a cavity referred to as Alcove 8 has been excavated within the Topopah Spring tuff upper

lithophysal zone (Tptpul). The Tptpul contains large lithophysae attributed to gas- and vapor-phase constituents entrapped and redistributed during the initial deposition, compaction, and gas migration out of the TSw [*Buesch and Spengler.*, 1998]. The highly fractured, welded TSw found at this depth lies within moderately-to-densely-welded ash-flow tuff [*Hinds et al.*, 2003]. While the Tptpul has fairly homogeneous matrix characteristics [*Flint*, 1998], line surveys by the U.S. Geological Survey (USGS) show significant variability, both in the frequency of fractures (i.e., mean and standard deviation of 0.8 ± 1.0 m^{-1}) and fracture lengths (i.e., from <1.0 m to 29 m). A map of the fractures visible on the floor of Alcove 8 is shown in Figure 1a. These fractures in the TSw are believed to have formed in response to cooling, gravitational unloading, regional stress, and faulting [*Hinds et al.*, 2003].

On the floor of Alcove 8, an area of 3×4 m^2 was delineated for liquid release. Along the perimeter of the plot, steel sheets were installed in grooves that had been chiseled along the floor. Similar sheets were used to divide the infiltration zone into 12 square plots of 1 m^2 (see Figure 1b). Because the sheets were sealed into the grooves, there was no lateral movement of water at the surface between subplots. To minimize losses through evaporation, each subplot was covered with a plastic sheet (see Figure 1b). In addition, the entire alcove was isolated from ventilation effects, associated with the adjacent drift, by bulkhead doors installed at the entrance to the alcove. These doors were opened only during routine maintenance of test equipment once or twice a week. As such, the microclimate within the alcove was relatively stable for the duration of the investigation, with the relative humidity remaining close to 100% when the doors to the cavity were closed.

Within the boundary of the infiltration zone, fractures were concentrated at the two ends, with few visible fractures in the middle (Figure 1a). The total length of visible fractures was largest in Subplot 12 (6 m) and smallest in Plot 6 (0.2 m), with an average of 1.9 m of fractures per subplot. The length and density of fractures identified within the subplots are presented in Table 1.

2.2. Liquid Release

Water used for this test originated from J-12 and J-13 wells at Yucca Mountain, and was spiked with about 20 mg/L LiBr. Chemical analysis of the J-13 well water showed that it contained 59 mg/L sodium, 5.9 mg/L potassium, 6.6 mg/L calcium, 0.50 mg/L magnesium, 3.3 mg/L silicon, 1.4 mg/L fluoride, 6.8 mg/L chloride, and 13 mg/L sulfate [*Hu et al.*, 2001]. It is unlikely that the chemical composition of the water significantly impacted the results of this investigation. For the duration of the experiment, each of the 12 subplots was irrigated independently with a designated water supply reservoir connected to a plastic tube, the end of which was fitted with a float valve. This float valve was set to automatically maintain the desired constant head by initiating flow from the supply tank as the head of water dropped a few millimeters below the prescribed head (see Figure 1b). The supply reservoir for each subplot was mounted on a scale that recorded the mass of water flowing into the subplots. Ponding of the initially dry surface began with 0.04 m^3 of water being pumped into the subplots (i.e., volume needed to reach the desired 0.04 m height of ponding). After this initial, rapid filling (20 minutes), an 0.04 m head of water was maintained in each of the 12 subplots.

Water was released in three distinct phases under ponded conditions into the infiltration plot over a period of 800 days. During Phase I, ponding of the entire plot began on August

20, 2002, and continued uninterrupted for 6 months. During Phase II, which began on March 24, 2003, and extended for six months, water was released into two of the subplots (i.e., 2 and 12) while the remaining 10 remained dry. Phase III began in early August 2003, when the release of water was resumed in all 12 subplots. During this phase, ponded conditions were maintained for 12 months, after which infiltration in six of the twelve plots was perturbed by a brief interruption to the water supply. In addition, the surface of the six plots was scrubbed to remove bio-film that had developed during the course of the infiltration experiment. The amount of water released, and the type of perturbation imposed on the subplots during the investigation, is summarized in Table 2.

3. Observations

3.1. Phase I Infiltration (Plots 1-12)

Phase I of the infiltration experiment extended over a period of 216 days, during which 21 m^3 of water was released onto the infiltration zone. The infiltration response measured at various locations along the plot suggests there was large spatial and temporal variability in the flow of water through the 3×4 m^2 surface (see Figure 2).

Spatial variability along the infiltration surface was apparent in the portioning of total water among the subplots. Relatively larger volumes of water were observed to infiltrate the northern and southern ends of the plot. The largest infiltration flux was measured in Subplot 2, which accounted for 30% of the water released. In Subplots 1, 10, 11, and 12, the percentage of total flux ranged between 9 and 18%, whereas in the seven remaining subplots, it was between 1 and 5 % (see Table 2).

Besides significant differences in the volume of water that infiltrated in each subplot, there was noticeable temporal variability in infiltration rates for some subplots, while in

others, infiltration rates remained relatively constant, as shown in Figure 2. Prominent in the temporal response was the pattern observed in Subplots 1, 2, 3, 10, and 11, where the infiltration rates continued to decrease during the first two weeks of ponding, rapidly increase to peak values in the next 2–3 weeks, and then sharply decrease before reaching relatively constant values. Unlike Subplots 1, 2, 3, and 11, the infiltration rate in Subplot 12 did not decrease rapidly after a maximum rate was achieved. In Subplots 4–9, the infiltration rates remained relatively low and relatively steady for the duration of the first phase of infiltration.

In Figure 3, the final infiltration rates observed at the end of Phase I in all the subplots are plotted against the total length of fractures in each subplot (Table 1). This figure shows a strong linear correlation between these two quantities (exception is Subplot 2). Assuming only the visible fractures are responsible for infiltration, this strong correlation implies that all the visible fractures have similar properties (i.e., aperture, roughness, and degree of infilling).

3.2. Phase II Infiltration (Plots 2 and 12)

Phase II of the test was designed to evaluate the impact of neighboring subplots on infiltration rates. To achieve this, at the start of Phase II, water was removed from 10 of the 12 subplots, whereas in the two Subplots with the highest near-constant infiltration rates (i.e., Subplots 2 and 12), ponding continued uninterrupted. For the duration of this phase, which extended for 157 days, this upper-boundary condition was maintained along the infiltration plot, as $\sim$1.88 m^3 and $\sim$1.4 m^3 of water moved through the surfaces of Subplots 2 and 12, respectively (see Figure 4).

When Phase II began, infiltration rates in Subplot 2 had dropped from a peak value of $\sim$ 100 mm/day to $\sim$ 15 mm/day. Associated with this drop was a large amount of variability in the daily infiltration rates (Figure 2), which persisted as the adjacent plots became dry (Figure 3). Similarly, in Subplot 12, infiltration rates observed towards the end of Phase I remained consistent for the duration of Phase II. These observations suggest that infiltration in these subplots was not likely impacted when the adjacent subplots were dried.

3.3. Phase III Response to Perturbations at the Infiltration Surface

Phase III of the infiltration test was configured to evaluate the impact of two specific perturbations on infiltration rates. The first perturbation involved terminating the supply of water to individual plots for varying periods. The second perturbation involved the removal of a thin layer of biofilm visible to the naked eye ($\sim$ 1 mm), which had appeared over the infiltration surface on 6 of the 12 subplots.

When ponded infiltration was resumed along the entire plot during Phase III, the surface of 10 of the 12 subplots had been dry for $\sim$5 months, while the remaining two, i.e., Subplots 2 and 12, had been dry for 3 weeks. With the resumption of ponding, infiltration rates in 9 subplots (i.e., 4–12) were found to be similar to those at the end of Phase I, as shown in Figure 5. It appears that during the long dry period, the near-surface hydrologic properties in these nine plots remained relatively unchanged, such that there was no measurable difference in the infiltration rates.

Subplots 1 and 2 were the only plots that showed some impact resulting from the dryout that preceded Phase III. In Subplot 1, the infiltration rate at the resumption of ponding was 30 mm/day, much higher than at the end of Phase 1, when it was 5 mm/day.

However, the higher infiltration rates did not persist, and the daily flux along this subplot rapidly approached a relatively steady rate of 10 mm/day. In Subplot 2, when water was re-introduced into the plot after 3 weeks of drying, the infiltration rates were initially slightly lower than at the end of Phase II (i.e., 12 mm/day, versus 14 mm/day), but steadily increased to 30 mm/day in the next 30 days. The infiltration rate then began to decline gradually, reaching a near-constant rate of 12 mm/day 200 days after Phase III ponding began.

When ponded water was briefly removed from Subplots 1, 6, 9, and 12 (734 days after the start of the infiltration experiment on 08/23/2004) there was no measurable difference in infiltration rates once ponding was resumed a few hours later. Similarly, in Subplots 3, 6, 9, and 12, infiltration rates did not change after the surface of each of these plots had been briefly scrubbed.

Subplots 1 and 2 were the only plots that showed a measurable response to scrubbing of their surfaces. Subplot 1, which had not shown any response to a brief interruption in the supply of ponded water, responded almost immediately after the surface had been cleaned. Here, the near-constant infiltration rate of 5 mm/day, which had persisted for over a year, rapidly increased to 70 mm/day and continued to increase over the next five days before peaking at 110 mm/day. After peaking, the infiltration rates then rapidly decreased over the next 30 days, during which ponded conditions were maintained on the plot.

In Subplot 2, the infiltration rate increased from 12 mm/day to 20 mm/day, immediately after the plot was scrubbed on Day 734 of the test. Following this steep increase, infiltration rates gradually increased to 30 mm/day in the next twelve days, and then

sharply to 70 mm/day over a period of nine days before dropping to 30 mm/day over a period of 24 hours. This dramatically reduced infiltration rate coincided with perturbations to the surface of Subplot 1. As the infiltration rates rapidly increased in Subplot 1, they dropped in Subplot 2, suggesting that there was some mechanism by which flow through the surface of Subplot 2 was reduced as the surface permeability of Subplot 1 was increased. The reduced infiltration rates in Subplot 2 persisted for the next 30 days, before gradually declining during the remaining few days of the test.

In summary, immediately after the surface of Subplot 1 was scrubbed (756 days into the infiltration test), there were two significant changes observed along the infiltration plot. In Subplot 1, there was an immediate increase in infiltration rates, from <5 mm/day to 70 mm/day, while in Subplot 2, which had been showing a continuous increase in infiltration rates over the preceding 3 weeks, there was an immediate decrease in infiltration rates.

4. Comparison with Classical Infiltration Models

The concept of infiltration and the associated mathematical expressions [e.g., *Green and Ampt*, 1911; *Kostiakov*, 1932; *Horton*, 1940; *Philip*, 1969] were originally developed to describe entry of water into soils. All these models capture the general trend of decreasing infiltration rate under ponded conditions. However, these models cannot be expected to describe water entry into a complex arrangement of fractures of various shapes and orientations. In this section, we compare the infiltration observation presented in the preceding subsections with the classical infiltration models, in order to provide the motivation for exploring some of the complicating factors that distinguish infiltration in fractured rocks from soils.

For illustrative purposes, we chose to compare the observed infiltration rates with the theoretical model of *Philip* [1969]:

$$i = i_c + \frac{s}{2\sqrt{t}} \tag{1}$$

where i and i_c are the instantaneous and steady-state infiltration rates, respectively, s is sorptivity of the soil, and t is time. Equation (1) assumes one-dimensional infiltration into homogenous, semi-infinite soil. For illustrative purposes, we ignored these assumptions and fitted Equation (1) to observed infiltration rates, with i_c and s optimized as fitted parameters. Comparisons between Equation (1) and infiltration rates observed in Plots 1 and 2 during Phase I are shown in Figure 6.

From these comparisons, it is evident that the classical infiltration models are not adequate to explain the observed infiltration behavior. Particularly, the rise of infiltration rate approximately 20 days after the test was started cannot be explained by the models. In Figure 6, the volume of infiltrated water not captured by the best-fit model (excess infiltration) is marked as a shaded region.

Note that for some of the subplots the observed infiltration rate patterns were virtually flat. For these subplots, we assumed that s is is so small that the infiltration rate according to Eq. (1) flattens before the first measured point. Hence, we were not able to quantify the excess infiltration. The best fit parameters of Eq. (1) and the percentages of excess infiltration are summarized in Table 3.

From these results, it is evident that, in at least half of the subplots, a significant portion of the total infiltration could not be predicted using the classical infiltration approach. In the subsequent section, we provide several possible explanations for these anomalies.

5. Potential Explanations for Infiltration Pattern Anomaly

The foregoing discussions demonstrated that the temporal pattern of long-term infiltration into fractured rock is significantly different from what is predicted by the classical infiltration models. In particular, we noted in at least six of the subplots (1, 2, 3, 5, 10, and 11) that the infiltration rate decreased for several days followed by gradual increase (in some cases to higher rates than the rate at the beginning of the test) and finally a slow decrease. The most remarkable change in infiltration rate was observed in Subplot 2 (Figure 6). Six days after the test began, the infiltration rate dropped to 6 mm/day when it started to increase again, reaching $>$ 100 m/day on Day 35 (an increase by a factor of $>$ 17). After Day 35, the infiltration rate decreased gradually and stabilized around 25 mm/day after Day 85 (a decrease by a factor of 0.25). In this section, we explore a few plausible scenarios that can explain these peculiar infiltration patterns.

Infiltration of water from a constant-head pond can be described in one-dimension using [*Richards*, 1931]

$$\frac{\partial \theta}{\partial t} = \frac{\partial}{\partial z}\left(K \frac{\partial}{\partial z}(h - z)\right) \tag{2a}$$

$$h = h_\circ < 0, \quad 0 \leq z \leq \infty, \quad t = 0 \tag{2b}$$

$$h = h_t > 0, \quad z = 0, \quad t > 0 \tag{2c}$$

where θ, h, and K are the water content, water potential, and hydraulic conductivity of the medium, respectively; $h_\circ$ and h_t are the initial and boundary water potentials, respectively; and z is a space coordinate positive downwards. At the top boundary ($z = 0$), the infiltration flux is

$$i = K_S(1 - \partial h/\partial z) \tag{3}$$

where we used $K = K_S$ to reflect that the top boundary is saturated. Therefore, any change in infiltration rate with time is related either to a change in the saturated hydraulic conductivity (K_S) or the water potential gradient ($\partial h/\partial z$). The classical models, as described in the introduction, are based mainly on the assumption that a decrease in water-potential gradient controls the transient phase of infiltration. This assumption is well fitting for a monotonously decreasing infiltration rate from ponded conditions. However, it is inadequate for explaining the increase in infiltration rate.

The large-magnitude fluctuations of infiltration rates observed during the course of this investigation can be explained by a number of mechanisms that increase or decrease the permeability of the fractured medium. These may include alterations of fracture aperture by clay swelling, erosion/deposition of infill, or dissolution/precipitation of fracture-surface minerals; enhancement or blockage of flow pathways by entrapped air or lithophysal cavities; and clogging of fractures by biological materials or translocated debris. In this paper, we discuss a five plausible mechanisms.

5.1. Clay Swelling

The absolute permeability (k) of the fracture tuff at the study site is largely controlled by the density and aperture of fractures. Fracture density cannot be expected to change significantly during the course of the infiltration test. However, it is likely for fracture aperture to increase significantly by the action of swelling of clayey infill.

Swelling (expansion) of clay is driven by the strong affinity for water of the interlayer spaces of the clay minerals. The overburden pressure P_{ob} (in excess of the bulk water at atmospheric pressure P_{atm}) that must be applied to prevent a saturated clay-water

mixture from further expanding is known as swelling pressure P_S,

$$P_S = P_{ob} - P_{\text{atm}} \tag{4}$$

Low [1980] examined the swelling properties of a wide range of clays and found that the dimensionless swelling pressure $\Pi = P_S/P_{\text{atm}}$ satisfies a dimensionless relation [*Murad*, 1999]

$$\Pi = \exp\left[\gamma\left(\frac{1}{w} - \frac{1}{w^*}\right)\right] - 1 = B\ e^{\gamma/w} - 1 \tag{5}$$

where w is the water ratio of the clay (which depends on the hydration state of the clay), w^* is the water ratio at $\Pi = 0$, γ is an empirical constant that ranges from 1.5 to 4.5, and $B = e^{-\gamma/w^*}$. Assuming that the clay swells only in the direction normal to the fracture plane, the water ratio is given by

$$w = \left(\frac{1}{1-\phi_\circ}\frac{b}{b_\circ} - 1\right)\frac{\rho_w}{\rho_p} \text{ for } b \geq b_\circ \tag{6}$$

where ρ_w and ρ_p are densities of water and the clay particles, $b_\circ$ is the initial fracture aperture, and $\phi_\circ$ is the initial porosity of the clay.

When clays expand within the confines of a fracture, the stiffness of the fractures imposes resistive force. Typically, stiffness of fractures is defined as

$$\sigma = E(b - b_\circ) \tag{7}$$

where E [MPa m^{-1}] is the stiffness coefficient. If a fracture is completely filled with swelling clay, then the fracture aperture will increase upon hydration of the clay if $P_S > \sigma$. Then, the maximum aperture can be calculated by equating Eqs. (5) and (7),

$$B\ \exp\left[\gamma\left(\frac{1}{1-\phi_\circ}\frac{b_{\max}}{b_\circ} - 1\right)^{-1}\frac{\rho_p}{\rho_w}\right] = \frac{E(b_{\max} - b_\circ)}{a\ P_{\text{atm}}} + 1 \tag{8}$$

where $a \leq 1$ accounts for the fact that the clay may fill only a small area of the fracture. Note that when the fracture is not completely filled with clay, there is a possibility for the

clay to swell within the fracture plane. In that case, significant fracture aperture increase cannot be expected. The calculations presented here imply that all the clay mineral layers are aligned with the fracture plane, such that swelling occurs predominantly normal to the fracture plane. Equation (8) must be solved iteratively because it involves $b_{\max}$ in nonalgebraic form.

In Figure 7, we show the ratio $b_{\max}/b_\circ$ as a function of $b_\circ$ for representative values of the parameters of Eq. (8) listed in Table 4. The rise in permeability that results from the increase in fracture aperture can be estimated using the cubic-law approximation ($k \propto b^2$),

$$k_{\max}/k_\circ = (b_{\max}/b_\circ)^2 \tag{9}$$

To achieve a 17 fold increase in permeability shown during the rise in infiltration rate in Subplot 2 (Figure 6b), the fracture aperture must increase by a factor of 4.12. In Figure 7, $b_{\max}/b_\circ = 4.12$ is shown as a horizontal dashed line. Given the parameters listed in Table 4 and the assumptions discussed above, Figure 7 suggests that clay swelling in fractures that are smaller than 0.1 mm can cause a fracture-aperture increase sufficient to explain the observed rise in infiltration rate.

5.2. Erosion of Fracture Infill

The portion of exposed fractures available to flow infiltration water can be significantly diminished if fractures are partially clogged by filling materials. Erosion of these fillings during infiltration could also be responsible for the gradual increase of the fracture portion available for infiltration. *Dahan et al.* [1999] demonstrated that infiltration into fractured chalk can be significantly influenced by dissolution of fracture walls and dislodging of

clogging materials, resulting in anomalous infiltration patterns that are similar to those reported herein.

For our purposes, we consider a single planar fracture of uniform aperture b with a fraction p of its lateral extent clogged by infills. Using the cubic-law approximation, the fracture permeability is given as

$$k \propto b^2(1-p) \tag{10}$$

Then, the impact of infill erosion on the fracture permeability can be estimated simply as

$$\frac{k(t)}{k_\circ} = \frac{1-p(t)}{1-p_\circ} \tag{11}$$

where $p_\circ$ and $k_\circ$ are the initial fracture filling fraction and the corresponding permeability, respectively, and $k(t)$ is the resulting time-dependent permeability increase.

Figure 8 depicts the permeability of a partially clogged fracture as a function of changing filling fraction p for different initial clogging conditions. The 17 fold increase in permeability observed during the rise in infiltration rate in Subplot 2 (Figure 6b) is shown as a horizontal dashed-line. From these results, it is apparent that erosion can play a significant role only if the initial degree of filling was high or when the infill and/or the fracture walls are easily erodible (e.g., limestones and similar soft rocks). The above model does not consider deposition of the eroded materials elsewhere within the fractured rock and the associated reduction of permeability [*Weisbrod et al.*, 2002, 1999]. Therefore, the net impact of erosion of filling materials in actual rocks is likely to be less marked than shown here.

5.3. Air Entrapment

Air entrapment during the first moments of infiltration and subsequent escape or dissolution could result in a late-time increase in infiltration rate [*Hillel*, 1998, see pp 421 and citations therein]. An obvious cause for air entrapment is when water infiltrates into a medium with a bottom boundary impervious to air, such as a shallow water table or clay lens. In our test site, the fractures are well connected, and the infiltration water appears unhindered about 20 m below the infiltration bed [*Salve*, 2005]. Therefore, this mechanism of air entrapment cannot be a principal cause for the observed rise in infiltration rate.

Another mechanism by which air may be trapped is the"occlusion (sealing off) of air by water obstructions arising in air-filled passages during an increase in water content" [*Stonestrom and Rubin*, 1989a, b]. This process can potentially trap large pockets of air surrounded by fast flow paths near the infiltration plot. Abrupt escape of such large pockets could lead to substantial increases in infiltration rate.

5.4. Effect of Lithophysal Cavities

The fractured tuff at the site is interspersed with lithophysal cavities that range in size from a few centimeters to about one meter. Entry of water into these cavities requires that they intersect one or more fractures that are actively involved in the infiltration process. In addition, the water pressure at the intersection must exceed some threshold, so that drops formed inside the cavity can start to grow and drip [*Or and Ghezzehei*, 2000]. The buildup of adequate pressure for water entry into a given cavity could occur well after the wetting front has bypassed the cavity. Then, the abrupt creation of a sink could potentially reverse the decrease in matric potential gradient. The significance of this process in causing anomalous infiltration requires further investigation.

5.5. Plugging by Surface Biofilm

The previous four subsections were concerned with mechanisms that can explain the increase in infiltration rate. This subsection deals with the subsequent decrease in infiltration rate. Experimental results presented in Subsection 3.3 showed that in Subplots 1 and 2, the infiltration rates increased immediately, from 5 mm/day to 70 mm/day and from 12 mm/day to 20 mm/day, respectively, after the beds of the infiltration subplots were scrubbed to remove visible biomass accumulation on the rock surface. These rapid increases suggest that the biological growth created a low-permeability mat.

In porous media, microbial cells could exist in suspension or firmly adsorbed to solid surfaces. When the environmental conditions are favorable, the adsorbed cells grow, increasing the amount of adsorbed biomass and thereby clogging the pore space available for transmission of fluids [e.g., see *Cunningham et al.*, 1991; *Rittmann*, 1993; *Taylor and Jaffe*, 1990]. *Cunningham et al.* [1991] conducted laboratory experiments in which biofilms were grown in synthetic porous media reactors. Nutrient-laden water was allowed to flow through the reactors under constant piezometric-head gradient. Detectable biofilms were observed two days after inoculation of the reactors, and the growth of the biofilms was stabilized after eight days at 60 μm. The permeability decreased rapidly during the period of increasing biofilm thickness and then stabilized in the range between 1 and 5% of the original (clean surface) value. Because our field experiments were neither inoculated nor enriched with nutrients, the rate of biofilm growth is expected to be slower than those reported by *Cunningham et al.* [1991]. Observable biofilm appeared in our test plots only after several weeks into the experiments.

6. Summary and Conclusions

Most of our current understanding of the infiltration process has been based on short-term episodes of precipitation, irrigation, or contaminant spills. However, in certain instances, infiltration can be a much longer process. For example, infiltration into fractured rock can occur over periods of weeks to months in watersheds located in semi-arid climate regimes. In such environments, where a soil mantle covers the underlying rock, precipitation originating as rain or snow saturates the overlying soil before infiltration into the bed rock commences. The latter process can take several weeks to months. In addition, recent observations and predictions of extreme precipitation events associated with global climate change suggest the inevitability of prolonged flooding and (subsequently) infiltration events that can continue for months.

In soils, infiltration-related mechanical changes, such as clay swelling and aggregate disintegration, tend to decrease permeability. These mechanical changes, in conjunction with a rapid decline in matric potential gradients, are responsible for the typically monotonous decline in infiltration rate described by most theoretical and empirical infiltration models.

In this paper, we presented that simple extensions of these soil infiltration models to prolonged infiltration into fractured rock could lead to significantly distorted predictions. The most distinct aspect of the observed infiltration patterns is the sudden surge in infiltration rates a few weeks after the tests started, although a relatively steady boundary condition was maintained. We hypothesized that this could be explained by an increase in fracture permeability during infiltration, which is contrary to what typically occurs during infiltration in soils. Potential causes for such an increase include swelling of clay fillings and erosion of loose filling debris.

In addition to temporal anomalies, our investigation indicates that infiltration rate into exposed fractures is characterized by strong spatial variability. This variability can be explained by the spatial patterns of fractures and fracture properties.

In summary, this study suggests that there is a significant gap in our knowledge of the infiltration process in fractured rocks, particularly over prolonged time scales. Furthermore, this study points to the need for a systematic study of infiltration into exposed fractured rock that accounts for spatial distribution of fractures and fracture properties, fracture fillings and their swell/shrink nature, and subsurface structures (such as cavities). An understanding of the infiltration process spanning weeks to months is key to developing management and recovery plans.

Acknowledgments. This work was supported by the Director, Office of Civilian Radioactive Waste Management, U.S. Department of Energy, through Memorandum Purchase Order QA-B004220RB3X between Bechtel SAIC Company, LLC, and the Ernest Orlando Lawrence Berkeley National Laboratory (Berkeley Lab). The support is provided to Berkeley Lab through the U.S. Department of Energy Contract No. DE-AC03-76SF00098. Thorough reviews and suggestions for improvement by Stefan Finsterle, Ming Zhu, John Nimmo and two anonymous reviewers are gratefully acknowledged. Editorial review by Daniel Hawkes is also acknowledged.

References

Albritton, D., et al., Technical summary, in *Climate Change 2001: The Scientific Basis. Contribution of Working Group I to the Third Assessment Report of the Intergovernmental Panel on Climate Change*, edited by Y. D. D. G. M. N. Houghton, J.T., K. M.

455 P.J. van der Linden, X. Dai, and C. Johnso, p. 881, Cambridge University Press,, Cam-
456 bridge, United Kingdom and New York, NY, USA, 2001.

457 Bai, M., F. Meng, D. Elsworth, Y. Abousleiman, and J.-C. Roegiers, Numerical modelling
458 of coupled flow and deformation in fractured rock specimens, *International Journal for*
459 *Numerical and Analytical Methods in Geomechanics*, *23*, 141–160, 1999.

460 Buesch, D., and R. Spengler., Detailed correlation of lithostratigraphic and borehole geo-
461 physical log data for identifying contacts at yucca mountain, in *International High-Level*
462 *Radioactive Waste Management Conference*, pp. 248–251, American Nuclear Society,
463 Le Grange Park, IL, 1998.

464 Cunningham, A. B., W. G. Characklis, F. Abedeen, and D. Crawford, Influence of biofilm
465 accumulation on porous-media hydrodynamics, *Environmental Science and Technology*,
466 *25*, 1305–1311, 1991.

467 Dahan, O., R. Nativ, E. M. Adar, B. Berkowitz, and Z. Ronen, Field observation of flow
468 in a fracture intersecting unsaturated chalk, *Water Resources Research*, *35*, 3315–3326,
469 1999.

470 Dahan, O., R. Nativ, E. M. Adar, B. Berkowitz, and N. Weisbrod, On fracture structure
471 and preferential flow in unsaturated chalk, *Ground Water*, *38*, 444–451, 2000.

472 Elrick, D. E., G. W. Parkin, W. D. Reynolds, and D. J. Fallow, Analysis of early-time
473 and steady-state single-ring infiltration under falling head conditions, *Water Resources*
474 *Research*, *31*, 1883–1893, 1995.

475 Faybishenko, B., R. Salve, P. Zawislanski, K. H. Lee, P. Cook, B. Freifeld, K. Williams,
476 and C. Doughty, Ponded infiltration test at the box canyon site: Data report and
477 preliminary analysis, *Tech. Rep. LBNL-40183,*, E. O. Lawrence Berkeley Natl. Lab,

1998.

Flint, L. E., Characterization of hydrogeologic units using matrix properties, yucca mountain, nevada, *Tech. Rep. Water Resources Investigations Report 97-4243*, U.S. Geological Survey, 1998.

Glass, R. J., M. J. Nicholl, A. L. Ramirez, and W. D. Daily, Liquid phase structure within an unsaturated fracture network beneath a surface infiltration event: Field experiment - art. no. 1199, *Water Resources Research*, *38*, 1199, 2002.

Green, W. H., and G. A. Ampt, Studies on soil physics part i - the flow of air and water through soils, *Journal of Agricultural Science*, *4*, 1–24, 1911.

Hillel, D., *Environmental Soil Physics*, Academic Press, San Diego, CA, 1998.

Hinds, J. J., G. S. Bodvarsson, and G. H. Nieder-Westermann, Conceptual evaluation of the potential role of fractures in unsaturated processes at yucca mountain, *Journal of Contaminant Hydrology*, *62-3*, 111–132, 2003.

Horton, R., An approach toward a physical interpreation of infiltration-capacity, *Proc. Soil Sci. Soc. Am.*, *5*, 399–417, 1940.

Hu, Q., R. Salve, W. Stringfellow, and J. Wang, Field tracer transport tests in unsaturated fractured tuff, *Journal of Contaminant Hydrology*, *51*, 1–12, 2001.

Kostiakov, A. N., On the dynamics of the coefficient of water percolation in soils and on the necessity for studying it from dynamic point of view for purpose of amelioration, in *Transactions 6th Congress International. Society of Soil Science, Part A*, pp. 7–21, Moscow, U.S.S.R., 1932.

Low, P. F., The swelling of clay .2. montmorillonites, *Soil Science Society of America Journal*, *44*, 667–676, 1980.

501 Murad, M. A., Thermomechanical model of hydration swelling in smectitic clays: Ii -
502 three-scale inter-phase mass transfer: Homogenization and computational validation,
503 *International Journal for Numerical and Analytical Methods in Geomechanics*, *23*, 697–
504 719, 1999.
505 Or, D., and T. A. Ghezzehei, Dripping into subterranean cavities from unsaturated frac-
506 tures under evaporative conditions, *Water Resources Research*, *36*, 381–393, 2000.
507 Philip, J. R., Theory of infiltration, *Advances in Hydrosciences*, *5*, 215–296, 1969.
508 Philip, J. R., Falling head ponded infiltration, *Water Resources Research*, *28*, 2147–2148,
509 1992.
510 Pilon, P. J., Guidelines for reducing flood losses, *Tech. rep.*, International Strategy for
511 Disaster Reduction, The United Nations, 2004.
512 Richards, L. A., Capillary conduction of liquids through porous mediums, *Physics*, *1*,
513 318–333, 1931.
514 Rittmann, B. E., The significance of biofilms in porous-media, *Water Resources Research*,
515 *29*, 2195–2202, 1993.
516 Salve, R., Observations of preferential flow during a liquid release experiment in fractured
517 welded tuffs, *Water Resources Research*, *41*, W09,427, doi:10.1029/2004WR003,570, 12
518 p., 2005.
519 Stonestrom, D. A., and J. Rubin, Air permeability and trapped-air content in 2 soils,
520 *Water Resources Research*, *25*, 1959–1969, 1989a.
521 Stonestrom, D. A., and J. Rubin, Water-content dependence of trapped air in 2 soils,
522 *Water Resources Research*, *25*, 1947–1958, 1989b.

Taylor, S. W., and P. R. Jaffe, Biofilm growth and the related changes in the physical-properties of a porous-medium .1. experimental investigation, *Water Resources Research*, *26*, 2153–2159, 1990.

Unger, A. J. A., B. Faybishenko, G. S. Bodvarsson, and A. M. Simmons, Simulating infiltration tests in fractured basalt at the box canyon site, idaho, *Vadose Zone Journal*, *3*, 75–89, 2004.

Weisbrod, N., R. Nativ, E. M. Adar, and D. Ronen, Impact of intermittent rainwater and wastewater flow on coated and uncoated fractures in chalk, *Water Resources Research*, *35*, 3211–3222, 1999.

Weisbrod, N., O. Dahan, and E. M. Adar, Particle transport in unsaturated fractured chalk under arid conditions, *Journal of Contaminant Hydrology*, *56*, 117–136, 2002.

Wood, T., and G. T. Norell, Integrated large-scale aquifer pumping and infiltration tests, groundwater pathways ou 7-06, summary report, *Tech. Rep. INEL-96/0256*, Idaho National Engineering and Environmental Laboratory, 1996.

Youngs, E. G., Developments in the physics of infiltration, *Soil Science Society of America Journal*, *59*, 307–313, 1995.

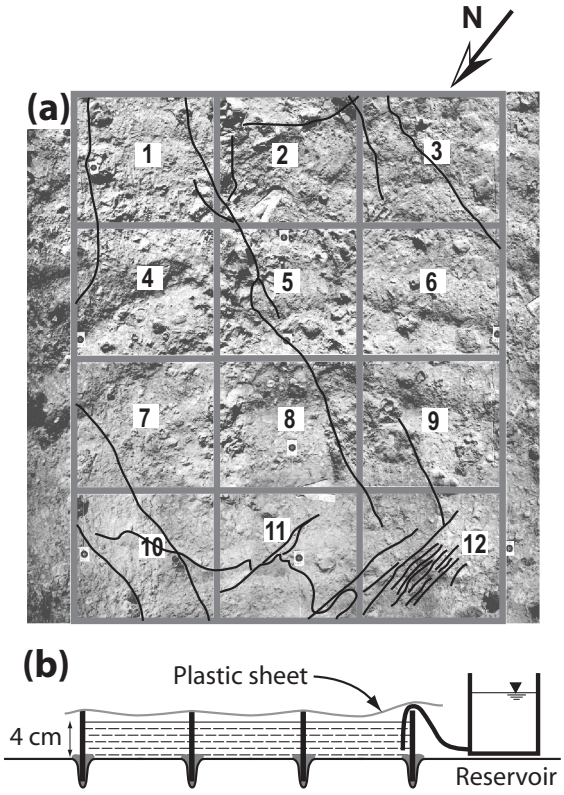

Figure 1. Schematic diagram showing (a) the fracture distribution near the infiltration plot and (b) a vertical crosssection of the infiltration plot. Note that subplots are 1 m^2

Table 1. Length and number of fracture sections observed in the infiltration zone. The total length is the sum of individual fractures found within each subplot.

Subplot	Number of Fracture	Length of Individual Fractures (m)	Total Length (m)
1	3	0.30, 0.60, 0.95	1.85
2	3	0.25, 0.60, 0.93	1.78
3	2	0.68, 1.16	1.85
4	1	0.68	0.68
5	2	0.38, 1.15	1.53
6	1	0.18	0.18
7	1	0.80	0.80
8	1	0.93	0.93
9	1	0.60	0.60
10	3	0.90, 1.08, 1.16	3.15
11	4	0.25, 0.43, 1.03, 1.63	3.33
12	14	0.15, 0.25, 0.25, 0.25, 0.30, 0.30, 0.38, 0.43, 0.50, 0.55, 0.55, 0.55, 0.55, 1.10	6.10

Table 2. Summary description of infiltration tests: duration, volumes of infiltrated water, and perturbations.

Plot	Phase I			Phase II			Phase III			
	Start	End	Infil	Start	End	Infil	Start	End	Infil	Perturbations
1	8/20/02	3/24/03	2135	3/24/03	8/28/03	0	8/28/03	10/18/04	11649	8/23/04 : E, R 9/13/04: E, S, R
2	8/20/02	3/24/03	6456	3/24/03	8/28/03	1910	8/28/03	10/18/04	8094	8/23/04: E, S, R
3	8/20/02	3/24/03	741	3/24/03	8/28/03	0	8/28/03	10/18/04	779	8/23/04 E, S, R
4	8/20/02	3/24/03	282	3/24/03	8/28/03	0	8/28/03	10/18/04	162	No perturbation
5	8/20/02	3/24/03	887	3/24/03	8/28/03	0	8/28/03	10/18/04	1059	No perturbation
6	8/20/02	3/24/03	429	3/24/03	8/28/03	0	8/28/03	10/18/04	447	8/23/04: E, R 9/13/04: E, S, R
7	8/20/02	3/24/03	472	3/24/03	8/28/03	0	8/28/03	10/18/04	347	No perturbation
8	8/20/02	3/24/03	890	3/24/03	8/28/03	0	8/28/03	10/18/04	471	No perturbation
9	8/20/02	3/24/03	687	3/24/03	8/28/03	0	8/28/03	10/18/04	426	8/23/04: E, R 9/14/04: E, S, R
10	8/20/02	3/24/03	2005	3/24/03	8/28/03	0	8/28/03	10/18/04	921	No perturbations
11	8/20/02	3/24/03	3704	3/24/03	8/28/03	0	8/28/03	10/18/04	1036	No perturbations
12	8/20/02	3/24/03	2654	3/24/03	8/28/03	1446	8/28/03	10/18/04	1220	8/23/04 E, R 9/14/04: E, S, R

KEY: Infil. = Infiltration Volume (m^3), E = emptied, R = Refilled, S = Scrubbed

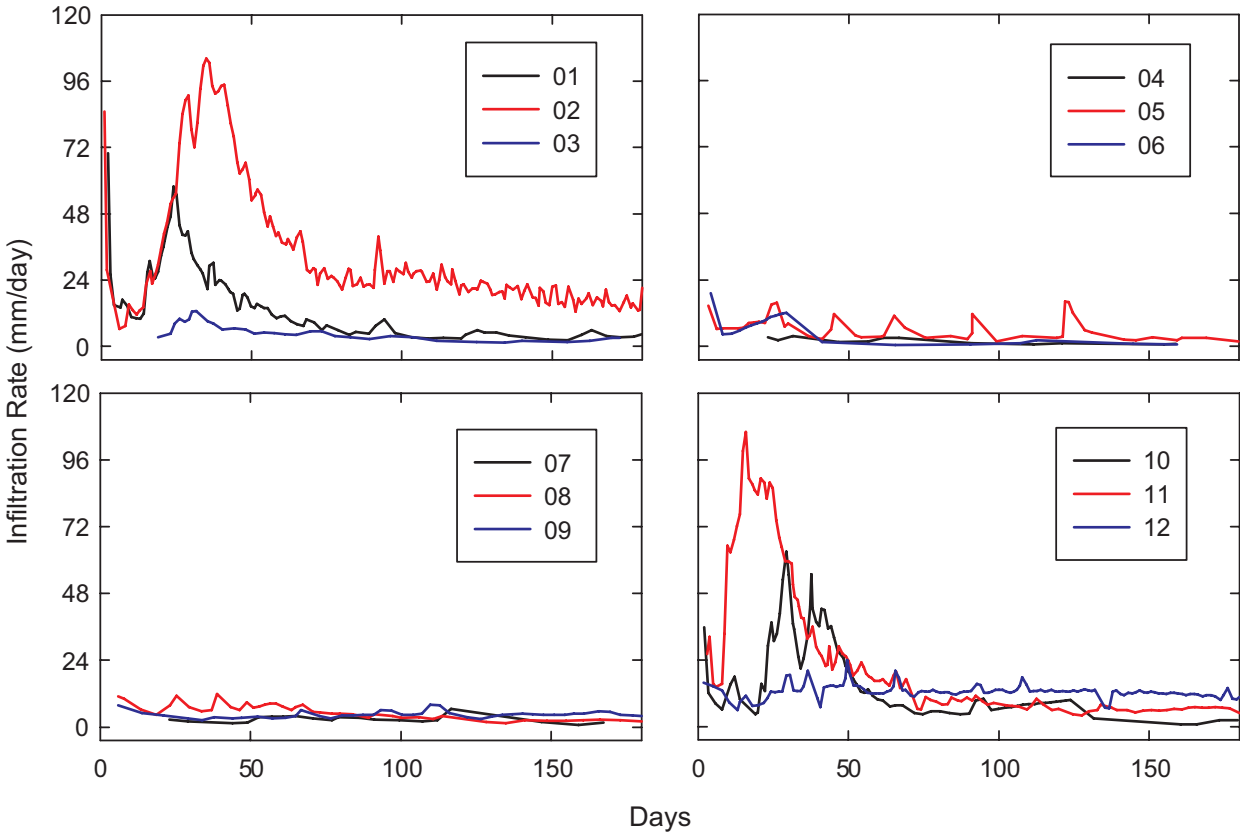

Figure 2. Results of Phase I infiltration test for all plots. Numbers on the legend correspond to subplot numbers shown in Figure 1. Days along the abscissa indicate the time since start of ponding on August 20, 2002.

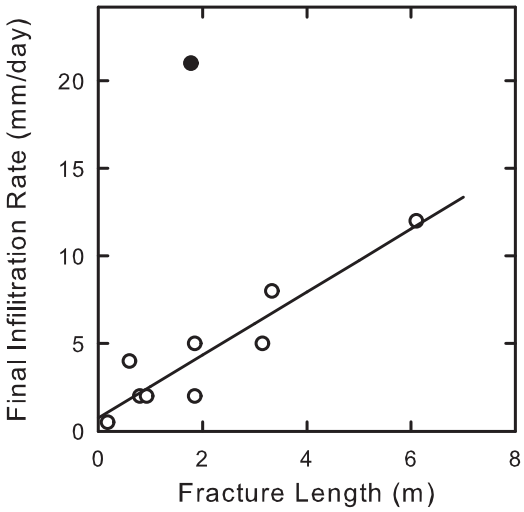

Figure 3. Correlation of final infiltration rate during Phase I with the fracture density (length). Filled circle denotes Subplot 2.

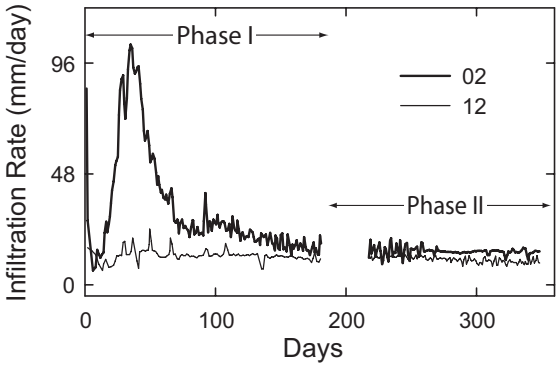

Figure 4. Results of phases I and II for Subplots 2 and 12.

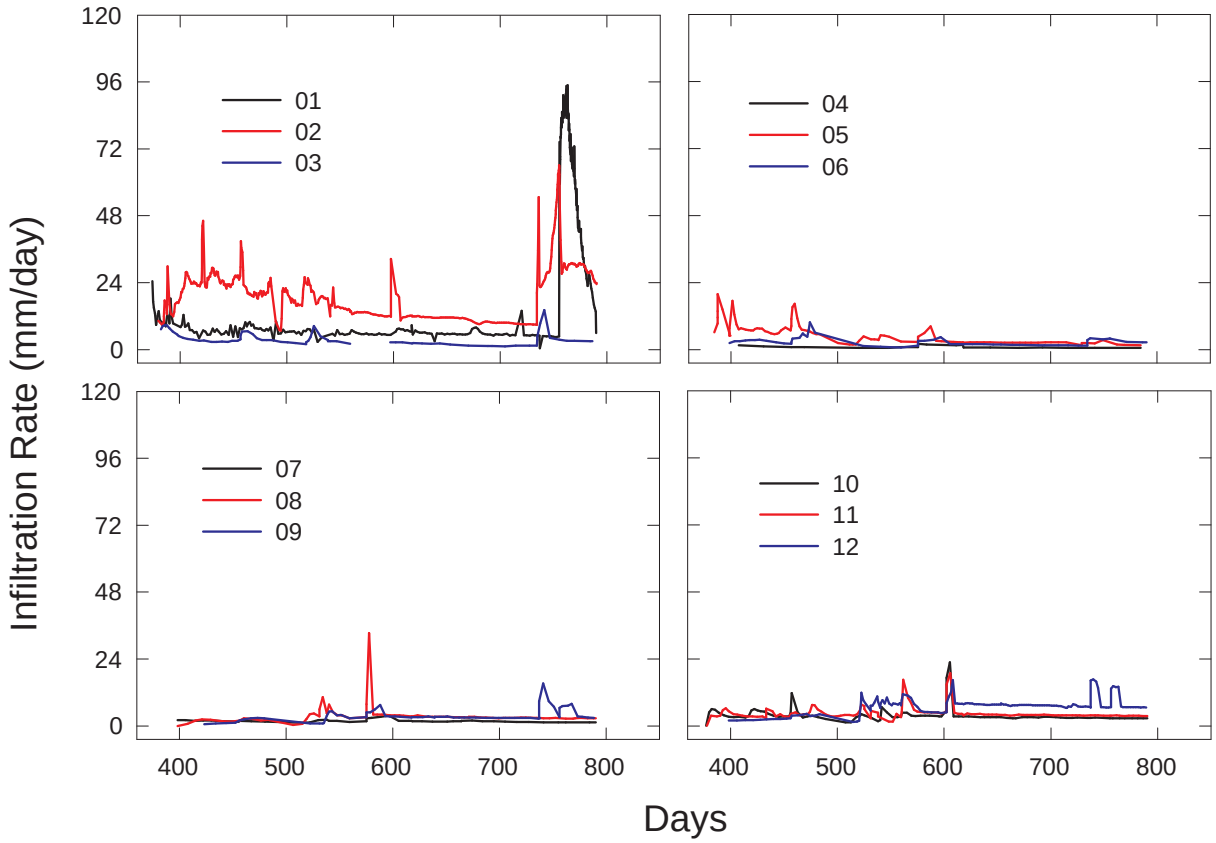

Figure 5. Results of Phase III infiltration test for all plots. Numbers on the legend correspond to subplot numbers shown in Figure 1. Days along the abscissa indicate the time since start of ponding on August 20, 2002.

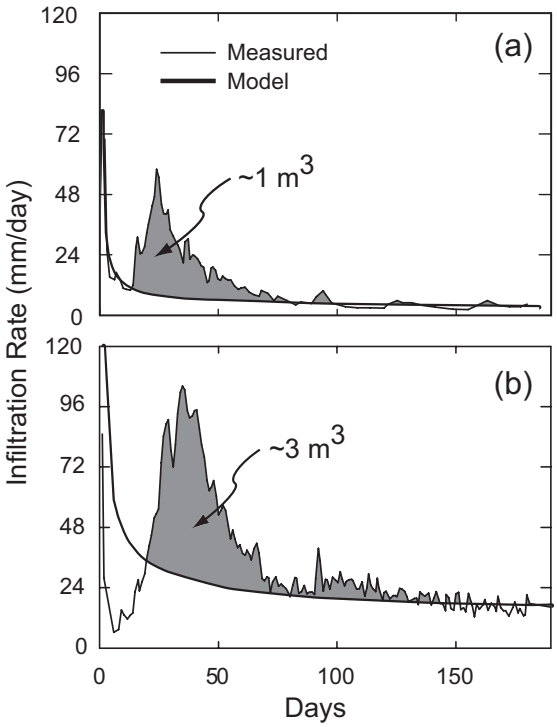

Figure 6. Comparison of the infiltration equation (1) with observed infiltration rates in (a) Plot 1 and (b) Plot 2, during Phase I.

Table 3. Percentage of the total infiltrated volume during Phase I that was in excess of the best-fit Philip's infiltration equation (1)

Subplot	i_c (mm/day)	s (mm/$\sqrt{\text{day}}$)	Excess Infiltration (%)
1	1.5	70	53
2	7.5	240	48
3	1.5	25	42
5	1.5	30	5
10	1.5	35	56
11	5.0	60	63

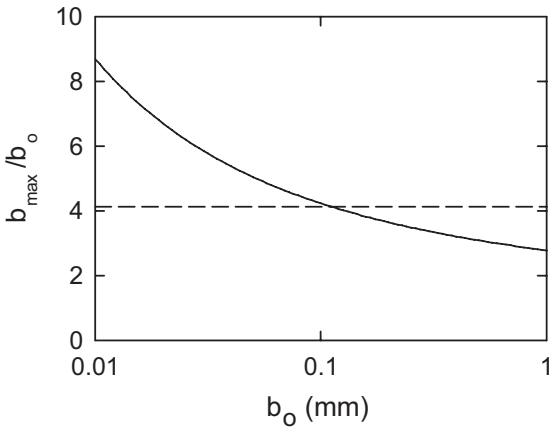

Figure 7. The maximum expected fracture aperture ($b/b_\circ$) as functions of the initial fracture aperture ($b_\circ$). Dashed line represents increase in fracture aperture by a factor of $\sqrt{17}$ needed to explain infiltration-rate rise in Subplot 2 during Phase I (see text for detailed explanation).

Table 4. Summary of parameters used in clay swelling illustrative example

Description	Symbol (unit)	Value
Empirical coefficient[a]	B	3
Empirical coefficient[a]	γ	2
Coefficient of Stiffness[b]	E (GPa/m)	1
Fraction of clay-filled fracture area	a	0.1
Clay porosity	ϕ	0.5
Density of water	ρ_w (kg/m^3)	1000
Density of clay minerals	ρ_p (kg/m^3)	2700

[a] Average swelling properties of montmorillonites derived from *Low* [1980]

[b] Stiffness of rock fractures derived from *Bai et al.* [1999]

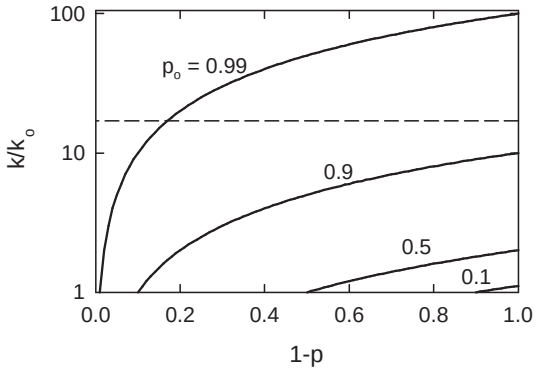

Figure 8. Impact of infill erosion on permeability of partially clogged fracture. Dashed line represents increase in fracture permeability by a factor of 17 needed to explain infiltration-rate rise in Subplot 2 during Phase I (see text for detailed explanation).